Mechanisms Controlling the Downstream Poleward Deflection of Midlatitude Storm Tracks

TALIA TAMARIN AND YOHAI KASPI

Department of Earth and Planetary Sciences, Weizmann Institute of Science, Rehovot, Israel

(Manuscript received 18 April 2016, in final form 2 October 2016)

ABSTRACT

The Atlantic and Pacific storm tracks in the Northern Hemisphere are characterized by a downstream poleward deflection, which has important consequences for the distribution of heat, wind, and precipitation in the midlatitudes. In this study, the spatial structure of the storm tracks is examined by tracking transient cyclones in an idealized GCM with a localized ocean heat flux. The localized atmospheric response is decomposed in terms of a time- and zonal-mean background flow, a stationary wave, and a transient eddy field. The Lagrangian tracks are used to construct cyclone composites and perform a spatially varying PV budget. Three distinct mechanisms that contribute to the poleward tilt emerge: transient nonlinear advection, latent heat release, and stationary advection. The downstream evolution of the PV composites shows the different role played by the stationary wave in each region. In the region where the tilt is maximized, all three mechanisms contribute to the poleward propagation of the low-level PV anomaly associated with the cyclone. Upstream of that region, the stationary wave is opposing the former two, and the poleward tendency is therefore reduced. Finally, through repeated experiments with enhanced strength of the heating source, it is shown that the poleward deflection of the storms enhances when the amplitude of the stationary wave increases.

1. Introduction

Midlatitude storm tracks and the weather systems that compose them control Earth's extratropical climate as they transfer heat, momentum, and moisture toward the poles. These weather systems are generated preferentially in the midlatitudes, specifically in regions where meridional temperature gradients are maximized (Peixoto and Oort 1992; Vallis 2006; Chang et al. 2002). In the Northern Hemisphere (NH), the two main storm tracks reside over the Pacific and Atlantic Oceans (Fig. 1). The localization of the storm tracks is mainly related to the ocean–continent temperature difference; it maximizes in the NH during winter (DJF; Fig. 1a), when relatively warm oceanic water meets the cold continent. The fewer number of continents in the Southern Hemisphere (SH) result in a single storm track that is more zonally symmetric. However, even in the SH, during winter (JJA; Fig. 1b), the storm track spirals toward the pole (Williams et al. 2007; Hoskins and Hodges 2005), which implies poleward deflection of the storms there.

Traditionally, there have been two complimentary approaches to study storm tracks. In a statistical time-mean approach, storm tracks are defined as regions where the atmospheric variability is maximized. A bandpass filter of 3–10 days is commonly used to determine the eddy fields, which can be applied to velocity, temperature, geopotential height, or any other field of interest (Blackmon et al. 1977). Derived eddy fluxes can then be obtained, and the eddy kinetic energy (EKE) distribution is frequently used to identify the storm tracks (Fig. 1). This approach is Eulerian in character, as it gives the local distribution of the eddy field (as measured in statistical equilibrium).

Alternatively, a Lagrangian approach to storm tracks employs a ''single-storm perspective,'' where storm tracks are defined as an ensemble of tracks of individual storms (e.g., Hoskins and Hodges 2002). One major advantage of the Lagrangian tracking approach is that it allows one to accumulate separate statistics for cyclones and anticyclones, which are indistinguishable in the statistical time-mean approach. This enables one to construct composites of cyclones and anticyclones throughout their track, which gives further information on their evolution, structure, and life cycle (e.g., Catto

Corresponding author e-mail: Talia Tamarin, talia.tamarin@weizmann.ac.il

DOI: 10.1175/JAS-D-16-0122.1

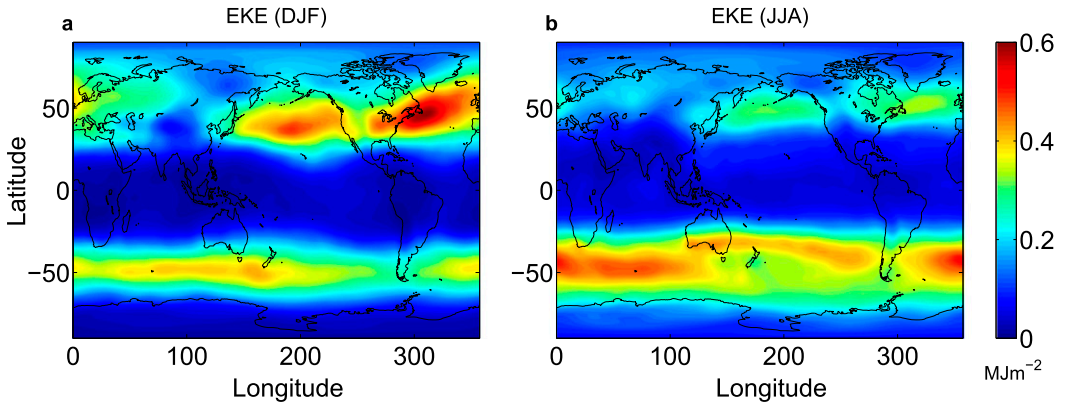

FIG. 1. Vertically integrated EKE (MJ m^{-2}) based on NCEP reanalysis data and calculated using a 3–10-day bandpass filter, averaged over the years 1970–2015 during (a) the NH winter (DJF) and (b) the SH winter (JJA).

et al. 2010). Several automated tracking algorithms have been developed in the past (e.g., Murray and Simmonds 1991; Hodges 1995; Blender et al. 1997; Sinclair 1997). The current study employs the feature-tracking algorithm developed by Hodges (1995), which was used previously in many studies of extratropical storms (e.g., Hoskins and Hodges 2002; Bengtsson et al. 2006; Catto et al. 2010; Harvey et al. 2012; Zappa et al. 2013).

An important feature of the localized storm tracks is their downstream poleward deflection, defined here as the deflection of the line of maximum EKE with respect to the zonal direction. The poleward deflection is most apparent during the NH wintertime (Fig. 1a) in the North Atlantic storm track, but it is also clearly apparent in the Pacific storm track (though it occurs farther downstream). The role of the stationary wave in the poleward tilt of the storm tracks was studied by various authors and attributed to zonal asymmetries, such as orography, and localized temperate gradients, such as land–sea contrasts and SST anomalies (e.g., Hoskins and Karoly 1981; Held 1983; Held and Ting 1990; Inatsu et al. 2002; Brayshaw et al. 2008; Kaspi and Schneider 2013). For example, it was shown that the presence of continents and mountains results in a storm track that is more tilted (Broccoli and Manabe 1992; Lee and Mak 1996; Brayshaw et al. 2009; Wilson et al. 2010). Other studies concentrated on the transient eddies and how their feedback with the mean flow shapes the storm track (e.g., Hoskins et al. 1983; Trenberth 1986; Hoskins and Valdes 1990; Orlanski 1998; Cai et al. 2007; Rivière 2009; Novak et al. 2015). Orlanski (1998) showed that the forcing by the high-frequency eddies is consistent with the poleward deflection; it produces a positive feedback with the stationary circulation, enhancing the trough at the storm-track entrance and the ridge at the storm-track exit region.

From a single storm perspective, it is known that the cyclones that compose the storm track tend to move on average toward the northeast direction, while anticyclones exhibit a more equatorward path (e.g., Petterssen 1956; Macdonald 1967; Klein 1957; Zishka and Smith 1980; Wallace et al. 1988; Blender et al. 1997; Mendes and Mendes 2004). This occurs even in the absence of zonal asymmetries (Tamarin and Kaspi 2016, hereafter TK16). Two dominant mechanisms were found to contribute to the poleward motion of midlatitude cyclones. The first mechanism is related to the nonlinear meridional advection of the lower-level cyclone induced from upper levels (Gilet et al. 2009; Rivière et al. 2012; Oruba et al. 2013; Coronel et al. 2015; TK16). This nonlinear advection is a result of the westward tilt with height that characterizes cyclones during their baroclinic growth stage. The vertical tilt implies that the low-level cyclone is located to the east of the upper-level trough, in a region where the upper-level velocity is oriented poleward. Thus, during the growth stage of the cyclone, the induced velocity from upper levels tends to advect it poleward. In addition, latent heat release (LHR) plays an important role in the poleward tendency of cyclones (Coronel et al. 2015; TK16). Cyclones are characterized by an inherent east–west asymmetry, since cyclonic motions transport warm and moist air to their east and cold dry air to their west. The warm and moist air to the east of the cyclone travels poleward and upward, forming part of the warm conveyer belt (Harrold 1973; Browning and Roberts 1994), and as it does so it cools and condenses. As a result, LHR maximizes on the northeastern side of the cyclone. This increases both the static stability and the absolute vorticity at lower levels, which result in a positive potential vorticity (PV) tendency at low levels (Davis et al. 1993; Stoelinga 1996; Ahmadi-Givi et al. 2004). Thus, a diabatically produced PV tendency is consistently formed at lower levels, propagating the PV anomaly eastward and poleward (TK16).

In this study, we extend the work by TK16, to include zonal asymmetries. There, we performed a PV tendency

analysis based on cyclone-tracking composites in an idealized zonally symmetric GCM. Here, we consider the case of a zonally asymmetric storm track by introducing a localized ocean heat flux, which results in enhanced baroclinicity downstream of the heating (e.g., Kaspi and Schneider 2011a, 2013). The PV analysis is thus modified to include the influence of the stationary circulation on the spatial downstream evolution of the storm track.

Studying the storm tracks from a statistical Eulerian perspective, in the time-mean equilibrium state, is important for understanding the balanced flow. However, it cannot give a complete understanding of how such a balance is achieved, as it is hard to determine cause and effect by simply comparing two balanced fields (i.e., deducing the role of the transient eddies in shaping the time-mean flow by looking at the balance between the eddy forcing and the mean-flow advection). Instead, here we perform the composites on the cyclones throughout their life cycle as they propagate downstream. This gives the actual instantaneous tendency, which can be decomposed into its separate contributions. Tracking the cyclones and analyzing their PV tendency instantaneously is therefore important for revealing the underlying mechanisms for their poleward motion.

The current paper is organized as follows. In section 2, a short description of the numerical methods is given. Section 3 presents the background flow, the tracking results, and the stationary–transient decomposition of the mean flow. In section 4, the downstream evolution of the composites over the stationary and transient velocities, as well as their associated PV anomalies, are presented. Section 5 presents the PV tendency analysis for the downstream region where the tilt of the storm track is maximized, while section 6 compares the downstream evolution of the dominant terms. The important mechanisms for the poleward tilt and the role of the stationary wave in each region are discussed. In addition, in section 7, we examine the relative role of the stationary circulation in the poleward tilt of the storm tracks by varying the strength of the localized heating source. Finally, conclusions and a summary are given in section 8.

2. Numerical methods

a. Idealized GCM

The idealized GCM used here is identical to that used in TK16, except for the inclusion of a localized asymmetry. The idealized GCM is based on NOAA's GFDL Flexible Modeling System (FMS), which is a three-dimensional model that solves the hydrostatic primitive equations for an ideal-gas atmosphere (Frierson et al. 2006; O'Gorman and Schneider 2008). The horizontal resolution used for this study is T85, corresponding to about 1.4° × 1.4°, and the vertical resolution includes 30 sigma levels ($\sigma = p/p_s$, where p_s is the surface pressure). The idealized model includes a simplified radiation scheme (Frierson et al. 2006) and a simplified representation of water vapor. A two-stream gray radiation scheme is used, with longwave optical thickness that depends only on pressure and latitude. Solar radiation is identical in both hemispheres (perpetual equinox conditions are used). A moist convection scheme relaxes the temperature of a convectively unstable parcel toward a moist adiabat with a time scale of 2 h, and the water vapor toward a fixed relative humidity of 70%. In addition, a grid-scale condensation scheme removes water vapor from the atmosphere whenever the specific humidity exceeds saturation (Frierson et al. 2006). The lower boundary of the model is water covered (a slab ocean), and its surface temperature evolves according to a surface energy balance, which includes thermal radiative fluxes and surface fluxes of latent heat and sensible heat. The idealized model does not include, for example, continents, clouds, aerosols, sea ice, and the diurnal and seasonal cycles. The model is first run for 2000 days to make sure that the system is in statistical equilibrium, and only then statistics are accumulated for another 3000 days.

To produce the localized storm tracks, which are the focus of this paper, we included a localized ocean heat flux in a square domain of length 10° in the midlatitudes, centered around latitude 40° and longitude 130° (thick small box in Fig. 2). The heating is introduced as an ocean heat flux (often referred to as Q flux) in the surface boundary condition of the slab ocean. It enters through the surface temperature tendency equation [e.g., Eq. (1) of Frierson et al. (2006)], as an additional anomalous heating on the right-hand side. The localized heating ideally represents the effect caused by land–ocean contrasts and the resulting western boundary currents (such as the Gulf Stream or Kuroshio), which transport warm ocean currents that enhance the temperature gradients and atmospheric heating during winter (Kaspi and Schneider 2011b). Note that a similar analysis can be done with other types of zonal asymmetries, such as continents or mountains (e.g., Held and Ting 1990; Brayshaw et al. 2009; Wills and Schneider 2015), or other forms of localized heating (e.g., Rivière 2009; Graff and LaCasce 2014).

b. Storm-tracking algorithm

The feature-point-tracking algorithm used in this study was developed by Hodges (1995). The tracking technique is performed on a sphere and involves minimizing a cost function for the ensemble track (by restricting changes in speed and propagation). The cyclones' centers in this study are identified by a minimum in the pressure field,

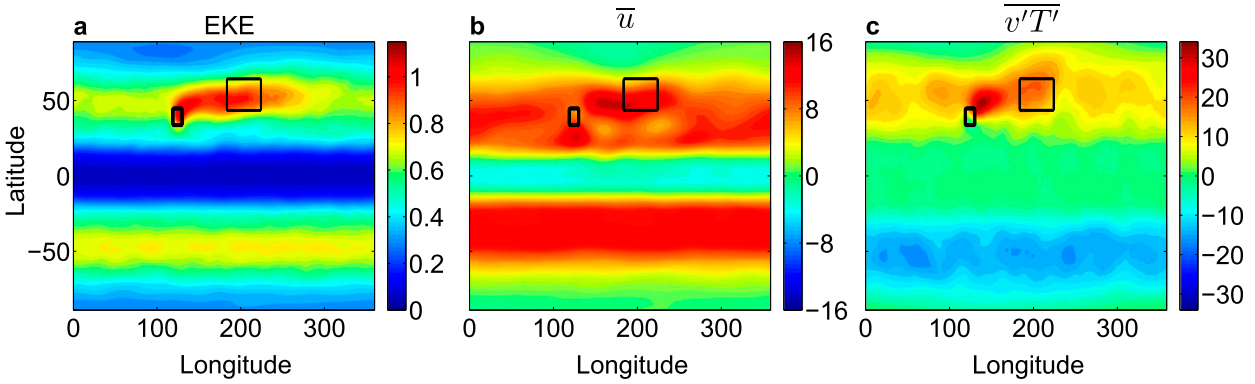

FIG. 2. Climatology of the simulation. Vertically (a) integrated EKE (MJ m^{-2}), (b) averaged zonal flow (m s^{-1}), and (c) averaged meridional heat flux (K m s^{-1}). In all the panels, the small black box shows the region where the localized ocean heat flux is applied, and the larger box shows the area where the downstream poleward deflection of the storm track is maximized (box C).

though tracking the vorticity field gives similar results. The background flow is removed before tracking is performed (all spatial wavenumbers ≤ 5), to isolate the synoptic-scale features. The fields are reduced to a T42 grid and then a spectral tapering is performed in order to suppress Gibbs phenomenon (Hodges 1995). The vertical level of $\sigma = 0.78$ is chosen here as representing the average of the lower layers (from $\sigma = 0.98$ to $\sigma = 0.5$), but similar results are obtained if the $\sigma = 0.85$ level is used instead. The storms are being tracked every six hours, and only mobile features traveling for more than two days are considered for the analysis. We use a cutoff of 1 hPa for identification of the pressure anomalies, but the results are insensitive to this cutoff value.

c. *Cyclone composites*

The tracking results are used to construct cyclone composites in different regions downstream of the localized heating source, as will be explained in more detail in section 4. For each cyclone, a box sized 30° in latitude by 40° in longitude around its center is used for the composite analysis. For each region, only the part of the track of cyclones whose center passes in that region is kept for the analysis. Any field of interest is then accumulated along the trajectory of the cyclonic storms (every 6 h, moving with the center of the cyclone) and then averaged together with all other tracks that passed in that region. Overall, in each composite representing a region, ~200 storms are averaged over the 3000 simulation days.

3. Stationary and transient decomposition

The localized heating results in a storm track that is tilted toward the pole (Fig. 2). A poleward deflection can be seen both in the transient field (Figs. 2a,c), where transient is defined here as deviations from the time mean, as well as in the downstream region of the time-mean zonal flow (Fig. 2b). The vertically integrated EKE in the NH (Fig. 2a) maximizes close to the heating box (small thick box) and deflects poleward when moving away longitudinally from the source. The tilt is largest close to the heating box (right to its east), but then a secondary deflection in the EKE is observed farther downstream (away from the heat source). This downstream deflection resembles more the structure observed in the Pacific storm track and is the focus of the current study. The big thin box in all panels of Fig. 2 marks this region where the downstream poleward tilt is maximized (later denoted as "box C"). Upstream of this region, the vertically averaged zonal flow appears to be much more zonally oriented, or even slightly deflected equatorward (Fig. 2b; see also Figs. 4a,d, which show only the stationary part of the flow). Interestingly, the vertically averaged poleward heat flux (Fig. 2c) has a secondary peak in this downstream region (box C).

To illustrate the similarities between the traditional approach of using Eulerian statistics and the feature-tracking approach that is adopted here, in Fig. 3a the actual tracks of cyclones at the $\sigma = 0.78$ level, which first appeared between latitudes 20° and 75° in the NH, are plotted (where color indicates the intensity of the system in units of hectopascals). Comparing the EKE (Fig. 2a) and the cyclonic tracks (Fig. 3a) shows clearly that in both cases there is an enhancement of the storms downstream of the localized heating. In addition, the poleward motion of cyclones downstream of the heating is strengthened. Translating to a common point all the tracks of cyclones that originated downstream of the heating box, between longitudes 120° and 210° (Fig. 3b), shows that the average cyclone in that region drifts approximately 13.9° in latitude poleward and 43.98° in longitude eastward (the cyclone drift is computed over the interval between the first and last detection of the cyclone). This gives a tilt angle of about 17.5°. On the

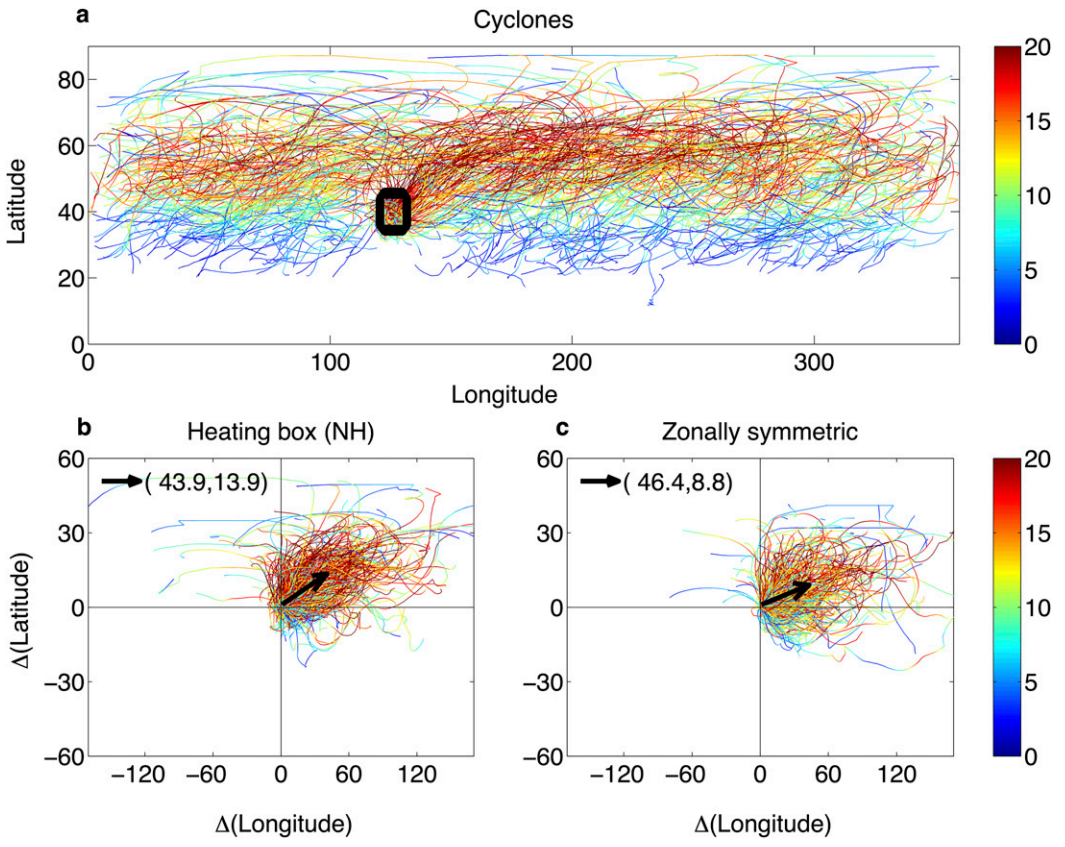

FIG. 3. (a) Tracks for lower-level (σ = 0.78) cyclones, with color indicating the intensity of the system (hPa). (b) Only the tracks that originated in the heating box [black thick box in (a)] translated to a common starting point. (c) Cyclones from a zonally symmetric run translated to a common starting point. Black arrows show the averaged cyclonic track for each case, and the numbers in the arrow legend denote the average longitudinal and latitudinal displacements, respectively.

other hand, translating to a common point all the tracks of cyclones for a case without a localized heating source (Fig. 3c) gives an overall averaged track of 8.88° in latitude poleward and 46.48° in longitude eastward. The resulting averaged track angle is much smaller, about 10.7°. Note that anticyclonic systems also compose the storm track, and hence the EKE, but these are not the focus of the current study, and hence their analysis is omitted here.

In TK16, we highlighted two dominant mechanisms responsible for the poleward motion of midlatitude cyclonic storms in the zonally symmetric case. The first results from a poleward advection of the low-level cyclones by the upper-level PV, as a result of the westward tilt with height that characterizes growing midlatitude cyclones. From a PV perspective, cyclogenesis can be explained by the interaction between an upper-level wave trough and a low-level PV anomaly. Growth is achieved when the phase difference between them is such that the upper trough is to the west of the low-level PV, and thus they are mutually amplifying each other by advecting the background PV (e.g., Martin 2006). In TK16 we emphasized that this configuration not only promotes growth, but also a poleward tendency at low levels, which is a result of the nonlinear advection of the low-level PV by upper-level PV. This was shown using a piecewise PV inversion technique (e.g., Davis and Emanuel 1991; Davis 1992), where the induced poleward winds from the upper-level PV were calculated explicitly.

The second important mechanism discussed in TK16 for the poleward motion of midlatitude cyclones is the release of latent heating. Since cyclones rotate anticlockwise in the NH (and clockwise in the SH), they systematically transfer poleward warm and moist subtropical air to their east. As this poleward moving warm and moist air expands upward adiabatically it cools, and water vapor condenses, releasing latent heat. Thus, LHR and consequent warming occur in the midtroposphere and peak to the northeast of the cyclone center. This can lead to both increased lower-tropospheric static stability (since isentropes are squeezed below the warming) and increased relative vorticity (since the warming enhances upward motion and therefore

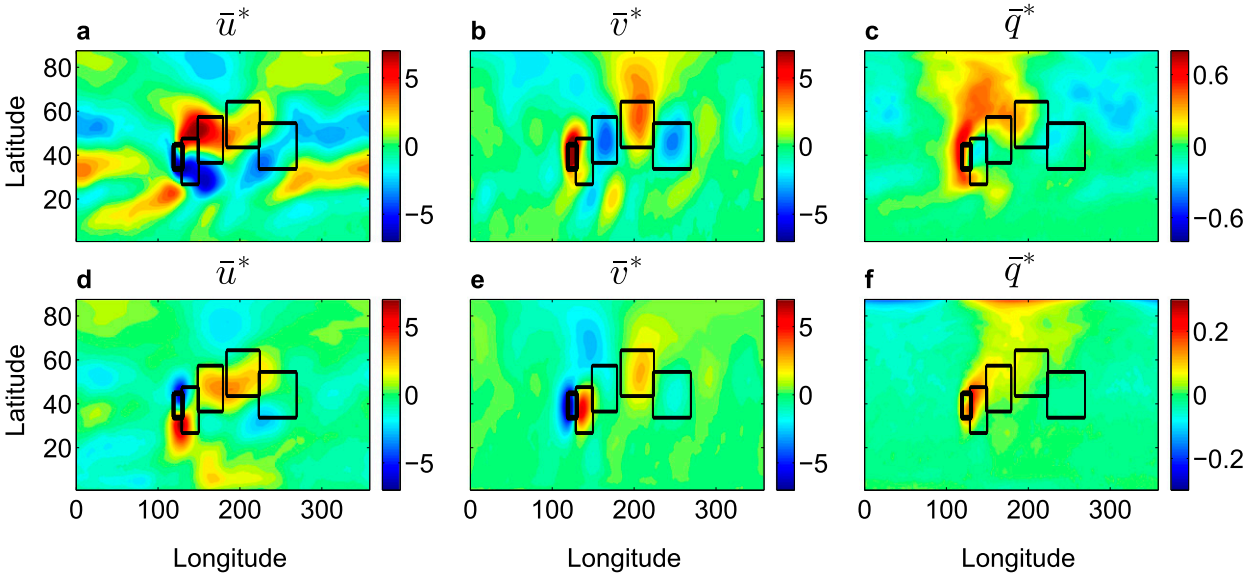

FIG. 4. The stationary part of the flow at (a)–(c) upper levels (σ = 0.3) and (d)–(f) lower levels (σ = 0.78). Shown are stationary (a),(d) zonal velocity (m s^{-1}), (b),(e) meridional velocity (m s^{-1}), and (c),(f) PV (PVU; 1 PVU = 10^{-6} K kg^{-1} m^2 s^{-1}). In each panel, the small thick box shows the region where the localized ocean heat flux is applied. The four larger and thinner boxes are the selected regions for further composite analysis.

convergence and cyclonic motion at lower levels). The two processes act to strengthen the low-level PV, which is proportional to their product. Thus, a positive PV tendency is constantly formed at lower levels, propagating the anomaly eastward and poleward. This is similar to the propagation mechanism of diabatic Rossby vortices (Parker and Thorpe 1995; Moore and Montgomery 2005; Moore et al. 2008, 2013), often used to explain their eastward tendency.

When a localized asymmetry is included, such as the localized ocean heat flux considered here, a stationary wave is formed (Held 1983; Held et al. 2002; Kaspi and Schneider 2011b). The stationary wave influences the dynamics and thus the track of the low-level cyclone. In this study, we repeat a similar analysis to that performed in TK16, except we now include the stationary part of the flow and examine how its contribution varies spatially. For this purpose, we decompose the flow into

$$a(x, y, p, t) = [\overline{a}](y, p) + \overline{a}^*(x, y, p) + a'(x, y, p, t), \quad (1)$$

where a is any field of interest. Here, an overbar represents time averaging, square brackets represent zonal averaging, a prime represents transient eddy (deviation from time mean), and the asterisk represents deviation from zonal mean.

The resulting stationary wave for our simulation is shown in Fig. 4. In all panels, the small thick square shows the heating box, and the four bigger boxes show the downstream locations chosen for further composite analysis. Downstream of the heating box, the stationary zonal flow anomaly at the upper level is positive to the north and negative to the south (Fig. 4a), suggesting a poleward jet shift in this region (consistent with Fig. 2b). At lower levels (σ = 0.78; Fig. 4d), the stationary zonal flow has a different structure. Close to the heating, a cyclonic stationary circulation is formed, opposite to the sign of the stationary zonal flow at upper levels. Downstream, however, the stationary zonal flow is similar to that seen in upper levels. At both heights, the third downstream box captures the region where the zonal flow is tilted poleward. The downstream regions are chosen to roughly collocate with the alternating sign of the stationary meridional velocity. At upper levels, the stationary meridional flow (Fig. 4b) is positive in the region of the heating box and then changes sign periodically over a finite region downstream. At lower levels (Fig. 4e), the stationary meridional velocity close to the heating box is consistent with a cyclonic circulation. Downstream, the stationary meridional velocity aligns with that of the upper levels (last three boxes). The stationary PV at the upper level (Fig. 4c) is characterized by a positive PV anomaly to the west of the heating box. In contrast, at lower levels (Fig. 4f) the stationary PV anomaly is to the east of the heating box and is stretched eastward and poleward.

In the following sections, we examine how the structure of the stationary wave presented above influences the transient eddies and their propagation by performing a composite analysis in each of the regions marked by the boxes. The structure of the stationary wave shown here is

consistent with stationary wave theory (e.g., Hoskins and Karoly 1981; Hoskins and Ambrizzi 1993; Ambrizzi and Hoskins 1997; Held et al. 2002). Assuming a stationary Rossby wave ($\omega = 0$) with dispersion $\omega = \overline{u}k - \beta^* k/K^2$, one finds a stationary wavenumber $K_s = \sqrt{\beta^*/\overline{u}}$. Here $\overline{u}$ is the mean westerly flow, $\beta^* = \beta - \partial^2\overline{u}/\partial y^2$, where β is the planetary vorticity gradient, and $K^2 = k^2 + l^2$ is the total wavenumber, where k and l are the zonal and meridional wavenumbers, respectively. On a sphere, the normalized stationary wavenumber becomes $K_s = \sqrt{\beta^*/\overline{u}}R\cos\phi$ (Hoskins and Karoly 1981; Hoskins and Ambrizzi 1993), where ϕ is the latitude and R is Earth's radius.

The third box, where the downstream tilt of the storm track is maximized, occurs approximately one stationary wavelength downstream of the heating (e.g., Fig. 4b). At latitude $\phi = 45°$ we find $\overline{u} \approx 18\,\mathrm{m\,s^1}$ and $\beta^* = 3.7 \times 10^{-11}$, which gives a total wavenumber of roughly 6.5. The wavelength in our experiment is approximately 80° of longitude, which corresponds to a normalized zonal wavenumber of 4.5. Assuming $k \sim l$, this gives a normalized total wavenumber of roughly 6.4, similar to the theoretical value. The arguments above imply that the stationary wavelength, and therefore the location of the region where the poleward tilt of the storm track is maximized, may be predicted based on linear arguments. However, the transient eddy field and the nonlinear interactions can obviously modify the stationary wave. In any case, the current manuscript does not focus on the stationary wave and its structure. Instead, the focus is on the influence of its structure, which is taken as given, on the transient eddies and their propagation within the storm track.

4. Composites and downstream evolution

In each downstream region marked by a box in Fig. 4 we perform a composite analysis (based on the tracking data shown in Fig. 3), as explained in the numerical methods section. The downstream evolution of the composites is shown in Fig. 5. The composites of the stationary part of the flow at low levels (Figs. 5a–c) resemble the stationary climatology within each region (Figs. 4d–f)[1]. In all the panels of Fig. 5, the black contours show the composite of the low-level transient PV anomaly associated with the cyclone, and the arrows show the stationary velocity at each region. Close to the heating area, in box A, there is a stationary cyclonic circulation (arrows in Figs. 5a–c, box A). The low-level stationary PV anomaly (Fig. 5c, box A) is centered around the low-level transient PV anomaly, though it is stretched in the southwest–northeast (SW–NE) direction.

Downstream of that, in box B, the stationary flow is mainly zonal (Figs. 5a,b, box B). The stationary PV anomaly (Fig. 5c, box B) is weaker and concentrated on the southwestward corner. Farther downstream, in box C, the stationary flow at low levels is both eastward (Fig. 5a, box C) and poleward (Fig. 5b, box C). In this region, the low-level cyclone and the associated transient PV anomaly reside between a stronger positive stationary PV to its west and a weaker negative stationary PV to its east (Fig. 5c, box C). Finally, in box D, the cyclone is already far from the heating source, and the stationary velocities are much weaker. The low-level transient PV anomaly is now at the edge of the stationary zonal jet (Fig. 5a, box D), in a region of weak equatorward velocity (Fig. 5b, box D). The low-level stationary PV is to the northwest of the cyclone, though it is much weaker now (Fig. 5c, box D).

Figure 5d shows the transient upper-level ($\sigma = 0.3$) PV anomaly and transient upper-level velocity (arrows). In all regions, the transient upper-level PV anomaly has a similar structure, and it is always to the west of the low-level transient PV anomaly (Fig. 5d, boxes A–D). However, moving downstream with the boxes (from box A to box C), the upper and lower transient PV anomalies appear to become more aligned.

The structure of the stationary circulation in the different regions described above will help us understand the observed stationary advection terms in the PV tendency budget. Performing the composites over the different regions is crucial when a localized zonal asymmetry is present, since the influence of the stationary wave is otherwise eliminated (if the composite is performed throughout the whole length scale of the storm track).

5. Composites of PV tendency

The tracking data are used to construct a composite of the PV budget. This is similar to the PV tendency analysis performed in TK16, except for the added contribution of the stationary field, and the necessity to develop composites over specific regions because of the stationary field.

In pressure coordinates, the Ertel PV is given by

$$q = -g(f\mathbf{k} + \nabla_p \times \mathbf{u}) \cdot \nabla_p \theta, \qquad (2)$$

[1] The composites of the stationary flow (Figs. 5a–c) are composites in the sense that they are calculated as an average of selected time steps, following the cyclones, though these are composites of fields that are stationary (zonal asymmetries of the climatological flow). They are averaged over each region and are therefore similar but not identical to the stationary time-mean field. For example, note that the sizes of the figures in Figs. 5a–c (L_x and L_y) are the latitude and longitude centered around each cyclone identified and not the sizes of the actual regions marked by boxes A–D (as in Fig. 4).

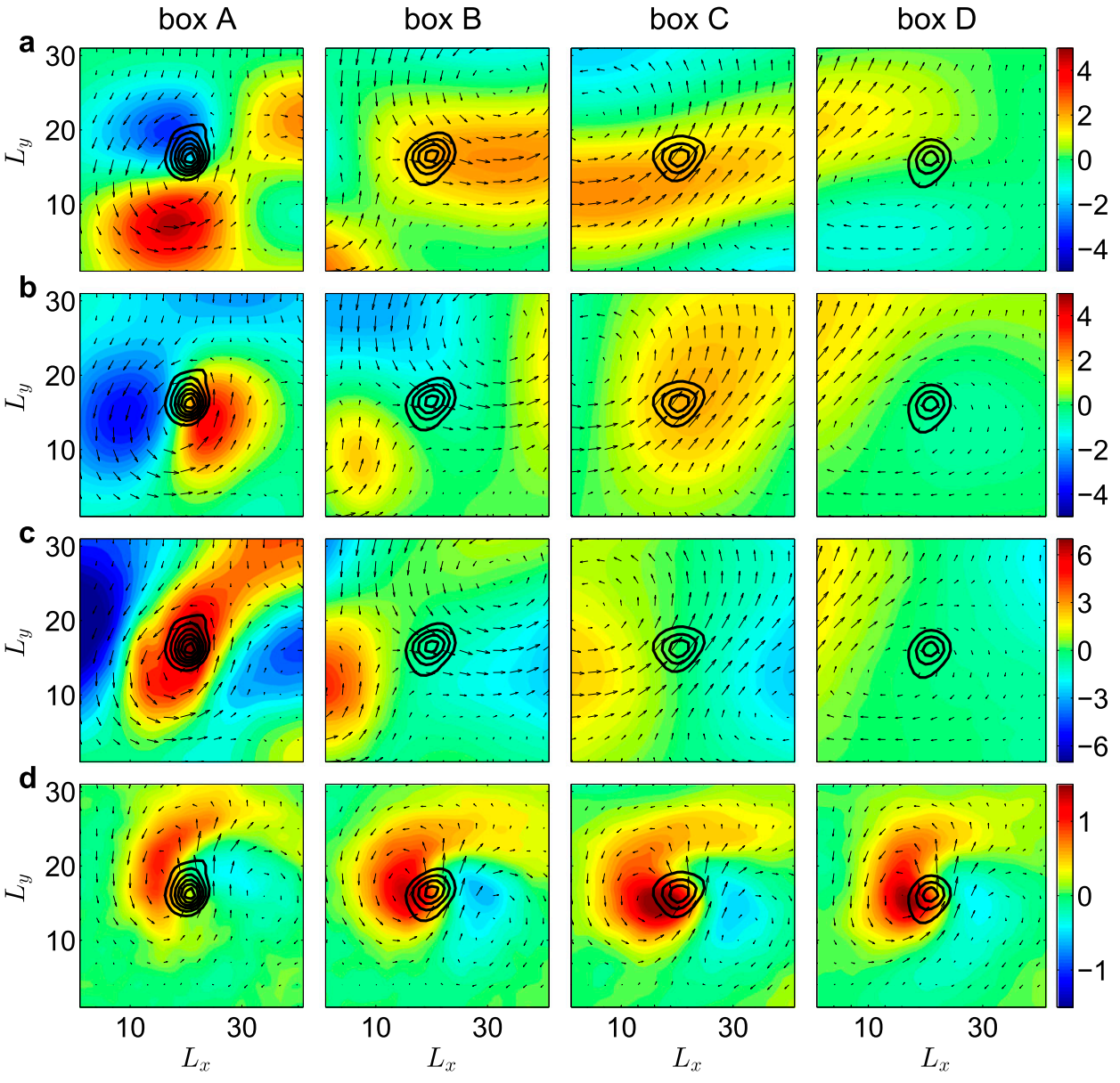

FIG. 5. Composites of the flow at different regions. Box A corresponds to the most upstream region (close to the localized heating), and box D corresponds to the most downstream region (farthest from heating). Shown are composites of the low-level ($\sigma = 0.78$) stationary (a) zonal velocity $\overline{u}^*$ and (b) meridional velocity $\overline{v}^*$ (m s^{-1}), (c) PV = $\overline{q}^*$ (10^{-1} PVU); and (d) composites of the upper-level ($\sigma = 0.3$) transient PV = q'(PVU). In (a)–(c), the arrows show the composite of the corresponding stationary velocities in each region, and in (d) the composite of the corresponding transient upper-level ($\sigma = 0.3$) velocities in each region. In all panels, the black contours show the corresponding low-level ($\sigma = 0.78$) transient PV anomaly (with lowest contour = 0.1 PVU, and contour intervals = 0.1PVU). The longitudinal and latitudinal extents of the composite are denoted by L_x and L_y, respectively. The maximum arrow magnitude in (a)–(c) is 4.8, 2.6, 2.8, and 2.1 m s^{-1} in boxes A–D, respectively, and in (d) is 12.6, 17.1, 16.9, and 17.6 m s^{-1} in boxes A–D, respectively.

where f is the planetary vorticity, $\nabla_p \times \mathbf{u}$ is the relative vorticity, $\nabla_p = (\partial/\partial x, \partial/\partial y, \partial/\partial p)$ is the gradient operator in pressure coordinates, and θ is the potential temperature. It satisfies

$$\frac{dq}{dt} = Q + F, \tag{3}$$

where $d/dt = \partial/\partial t + u\partial/\partial x + v\partial/\partial y + \omega\partial/\partial p$ is the material derivative and $\omega = dp/dt$. The right-hand side includes a friction term F, which is neglected here (at the level of $\sigma = 0.78$), and diabatic heating, which includes LHR and radiation and is given by

$$Q = -g(f\mathbf{k} + \nabla_p \times \mathbf{u}) \cdot \nabla_p(d\theta/dt). \tag{4}$$

In the absence of friction ($F = 0$), adiabatic motion ($Q = 0$) will conserve its PV Lagrangianly ($dq/dt = 0$).

Using the decomposition given in Eq. (1), the PV tendency Eq. (3) becomes[2]

$$\frac{\partial q}{\partial t} = -[\overline{u}]\frac{\partial q'}{\partial x} - u'\frac{\partial q'}{\partial x} - \overline{u}^*\frac{\partial q'}{\partial x} - [\overline{u}]\frac{\partial \overline{q}^*}{\partial x} - u'\frac{\partial \overline{q}^*}{\partial x} - \overline{u}^*\frac{\partial \overline{q}^*}{\partial x}$$
$$- v'\frac{\partial [\overline{q}]}{\partial y} - v'\frac{\partial q'}{\partial y} - \overline{v}^*\frac{\partial q'}{\partial y} - \overline{v}^*\frac{\partial [\overline{q}]}{\partial y} - v'\frac{\partial \overline{q}^*}{\partial y} - \overline{v}^*\frac{\partial \overline{q}^*}{\partial y} - \omega\frac{\partial q}{\partial p} + Q. \quad (5)$$

For simplicity we used here Cartesian notation (x, y), but all calculations are done in spherical coordinates. Note that the meridional background flow $[\overline{v}]$ is small (two orders of magnitude smaller than the leading terms), and its analysis was therefore omitted here.

We first concentrate on box C, which is the region where the downstream poleward tilt of the storm track is maximized (see Fig. 2 and Fig. 4), and then compare selected terms from the PV tendency budget for all regions in section 6. The total PV tendency budget is summarized in Fig. 6. The instantaneous PV tendency ($\partial q/\partial t$; Fig. 6a) shows that the overall structure is indeed tilted in the SW–NE direction. Hence, on average, the cyclone and its associated low-level PV anomaly move toward the northeast direction. We then decompose the instantaneous PV tendency into its different components, using the right-hand side of Eq. (5), to find explicitly which terms contribute to the SW–NE tilt and therefore to the poleward propagation. The PV tendency from diabatic heating due to LHR (Fig. 6b) is positive mainly over the warm sector of the cyclone and maximizes in the northeastern side of the low-level PV, and thus it contributes significantly to the poleward propagation of the low-level cyclone. As was explained in TK16, this occurs since LHR systematically produces a positive PV tendency in the northeastern side of the low-level PV. The contribution of the diabatic term due to radiation (Fig. 6c) gives a weaker negative PV tendency. The vertical advection of the transient PV anomaly gives a mostly negative PV tendency (Fig. 6d), concentrated in the southeastern side of the low-level PV. The latter two terms obviously do not contribute to the poleward tendency.

The sum of the horizontal advection terms (Fig. 6e) also gives a SW–NE-tilted PV tendency. The full decomposition of the horizontal advection is given in appendix A, where we show explicitly each of the zonal (Fig. A1) and meridional (Fig. A2) advection terms. Breaking this term into advection of the transient perturbation by the time and zonal mean (Fig. 6f), the transient field itself (Fig. 6g), and the stationary field (Fig. 6h) shows the first is dominating the eastward advection, while the latter two contribute to the poleward propagation and are of similar order (note that the colorbar scale in the last two panels is smaller than the previous panels).

Three processes are therefore responsible for the poleward tendency felt by the low-level cyclones in the downstream region of box C; PV tendency due to diabatic processes associated with LHR, nonlinear advection of the transient PV by its own field (induced from upper levels, as explained in TK16), and a stationary poleward advection.

The first two mechanisms discussed above are identical to those found in the zonally symmetric case considered in TK16. There the dynamics were simpler because the PV composites did not vary much throughout the track of the cyclones (during the growth stage of the cyclones). Here, there is an additional complication due to the spatial dependence and downstream evolution of the storm track. Nonetheless, these basic mechanisms appear to contribute in a similar manner to the poleward motion of the low-level cyclones.

The third mechanism discussed here, the stationary poleward advection of the transient PV, appears only in the zonally asymmetric case. Its amplitude depends on the strength of the stationary wave, and hence on the strength of the zonal asymmetry (see Fig. 9 in section 7, where we systematically vary the strength of the localized heating source). The fact that in this region the advections by the stationary and the transient anomalies both act in the same direction (Figs. 6g,h) is responsible for the strong poleward tilt and enhanced poleward motion seen in this region. As shown next, this is not the case for all the downstream regions of the storm track.

6. Downstream evolution of the PV tendency

In this section, the PV analysis of the previous section is repeated for the dominant terms in the PV budget at

[2] Note that the left-hand side of Eq. (5) satisfies by definition $\partial q/\partial t = \partial q'/\partial t$. However, the right-hand side of Eq. (5) also includes terms that involve only the stationary wave. These do not influence directly the PV tendency of the transient anomaly $\partial q'/\partial t$, but rather they cancel out with the time-mean value of Q. These terms are small and negligible in comparison to the terms involving the transient anomaly, as shown in appendix A.

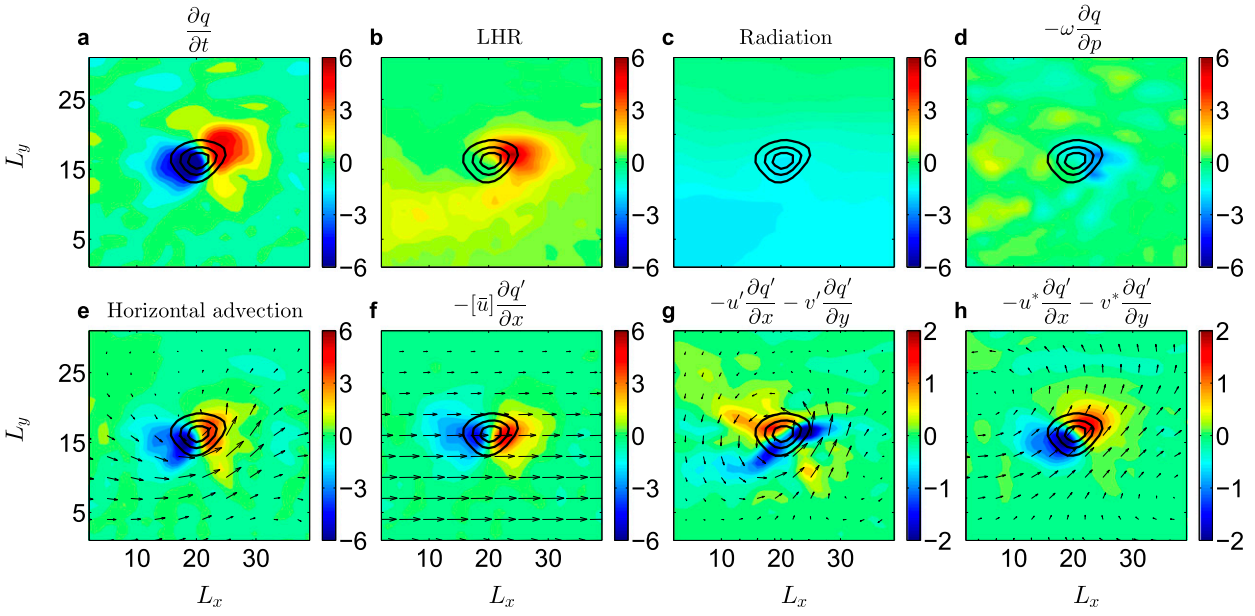

FIG. 6. The low-level ($\sigma = 0.78$) composites in box C of PV tendencies: (a) instantaneous $\partial q/\partial t$, (b) due to diabatic processes associated with latent heat release, (c) due to diabatic processes associated with radiation, and (d) from vertical advection. (e) The PV tendency from horizontal advection terms (sum of terms in Figs. A1 and A2 in appendix A), and (f)–(h) decomposition of this term into horizontal advection of the transient PV by the following: (f) the background time- and zonal-mean flow, (g) the transient velocity, and (h) the stationary velocity. In (e)–(h), the arrows show the corresponding velocity field. All quantities are normalized by 10^{-6} PVU s^{-1}. The black contours show the low-level ($\sigma = 0.78$) transient PV anomaly (with lowest contour = 0.1 PVU and contour intervals = 0.1 PVU). The longitudinal and latitudinal extents of the composite are denoted by L_x and L_y, respectively. The maximum arrow magnitude in (e)–(h) is 20.6, 7.1, 13.8, and 2.8 m s^{-1}, respectively.

different spatial locations downstream of the localized heating. Comparing the PV tendency of the storms as they move downstream, at different locations, allows for understanding of how each component of the flow influences the cyclone instantaneously throughout its track. This is especially crucial for the stationary advection, which varies significantly from one region to another.

Close to the heating box (box A), the PV tendencies are, in general, strongest, and they become weaker moving away from the heating box (boxes B–D). Note that the color scale in each row of Fig. 7, which corresponds to different PV tendency terms, is different (since weak fields would have otherwise been obscured). The instantaneous PV tendency ($\partial q/\partial t$; Fig. 7a) is characterized by a SW–NE tilt in all the boxes. However, the tilt is less pronounced in box B (where the zonal flow appears to be more zonal: e.g., Fig. 4), and then increases again downstream (boxes C and D in Fig. 7a).

The diabatic PV tendency due to LHR (Fig. 7b) is always positive in the northeastern side of the low-level PV anomaly. However, as the cyclones move downstream, the positive PV tendency becomes weaker and smaller. This is probably because, close to the localized ocean heat flux, both the LHR and the PV anomaly itself are larger.

The nonlinear transient PV advection by the transient wind field (Fig. 7c) gives a poleward and slightly westward tendency, except in box A, where it is equatorward and eastward. In boxes B–D, the transient nonlinear PV tendency does not vary much when the cyclone moves downstream, and it is similar to what was found in the zonally symmetric case considered in TK16. In these cases, the low-level PV is influenced by the upper-level PV (see Fig. 5d). Since the upper transient PV anomaly is always to the west of the low-level transient PV anomaly, positive meridional winds are induced from upper levels, advecting the low-level cyclone poleward.

Close to the heating source, in box A, the low-level PV is stronger than in the other downstream regions and is comparable in magnitude to the upper-level PV (which is usually stronger). This is probably a result of strong diabatically produced near-surface PV, as a result of the proximity to the heat source. Hence, cyclogenesis at the entrance of the storm track is dominated by diabatic processes, with a strong low-level PV and a weaker signature from the upper-level PV. Equatorward PV tendency induced by low-level winds was found both in Coronel et al. (2015) (see Fig. 6c there), where it was attributed to the low-level PV, and in TK16 (see Fig. 8c there), where it was attributed to the surface PV. The horizontal advection at the entrance of the storm track is therefore dominated by low-level

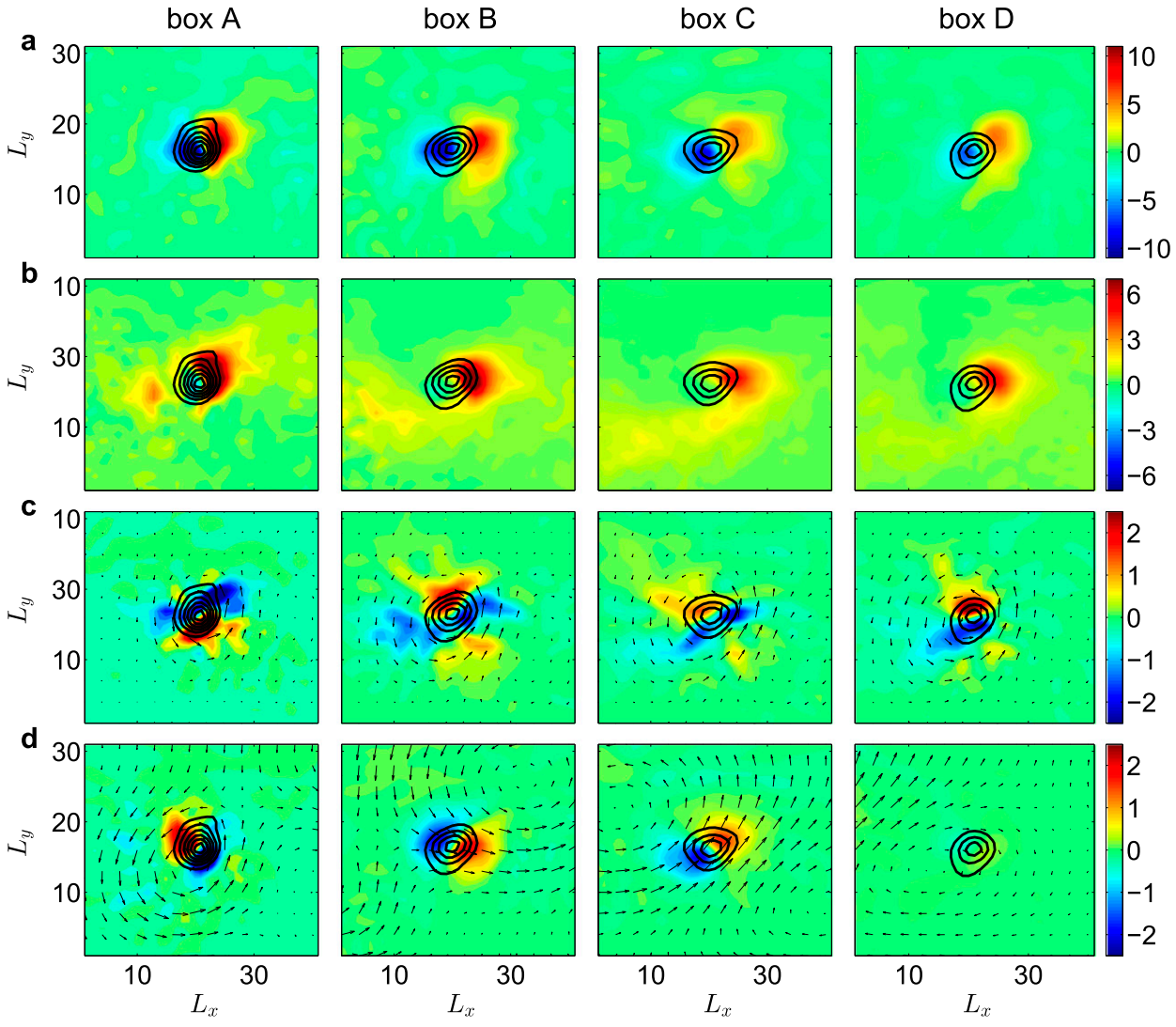

FIG. 7. Composites of selected low-level ($\sigma = 0.78$) PV composites at different regions. Box A corresponds to the most upstream region (close to the heating), and box D corresponds to the most downstream region (farthest from heating). Shown are (a) instantaneous PV tendency $\partial q/\partial t$, (b) PV tendency associated with latent heat release, (c) transient horizontal advection of the transient PV anomaly, and (d) stationary horizontal advection of the transient PV anomaly. In all panels, the black contours show the corresponding low-level transient PV anomaly (with lowest contour = 0.1 PVU and contour intervals = 0.1 PVU). In (c) and (d), the black arrows show the corresponding velocities from the composite in that region. The longitudinal and latitudinal extents of the composite are denoted by L_x and L_y, respectively. The maximum arrow magnitude in (c) is 13.7, 14.9, 13.8, and 13.7 m s^{-1} in boxes A–D, respectively, and in (d) is 4.8, 2.6, 2.8, and 2.1 m s^{-1} in boxes A–D, respectively.

advection, which gives rise to an overall equatorward advection (Fig. 7c, box A).

The influence of the stationary flow (Fig. 7d) changes significantly throughout the downstream development of the cyclone. Close to the heating box (Fig. 7d, box A), the stationary circulation (which is cyclonic) tends to advect the transient PV northwestward. Downstream of that (Fig. 7d, box B), the stationary circulation advects the cyclones southeastward. This opposes the northwestward advection associated with the transient nonlinear term, and as a result the overall PV tendency is more zonal in that region (Fig. 7a, box B). Farther downstream (Fig. 7d, box C), as discussed in the previous section, the stationary flow tends to advect the cyclone toward the northeast. This, combined with the northwestward tendency from the transient nonlinear advection terms, gives an overall strengthened poleward tendency. This is consistent with the enhanced poleward tilt seen in box C (e.g., Fig. 4). Finally, in box D (Fig. 7d, box D), the stationary PV advection is much weaker, and is oriented again to advect the low-level cyclone equatorward.

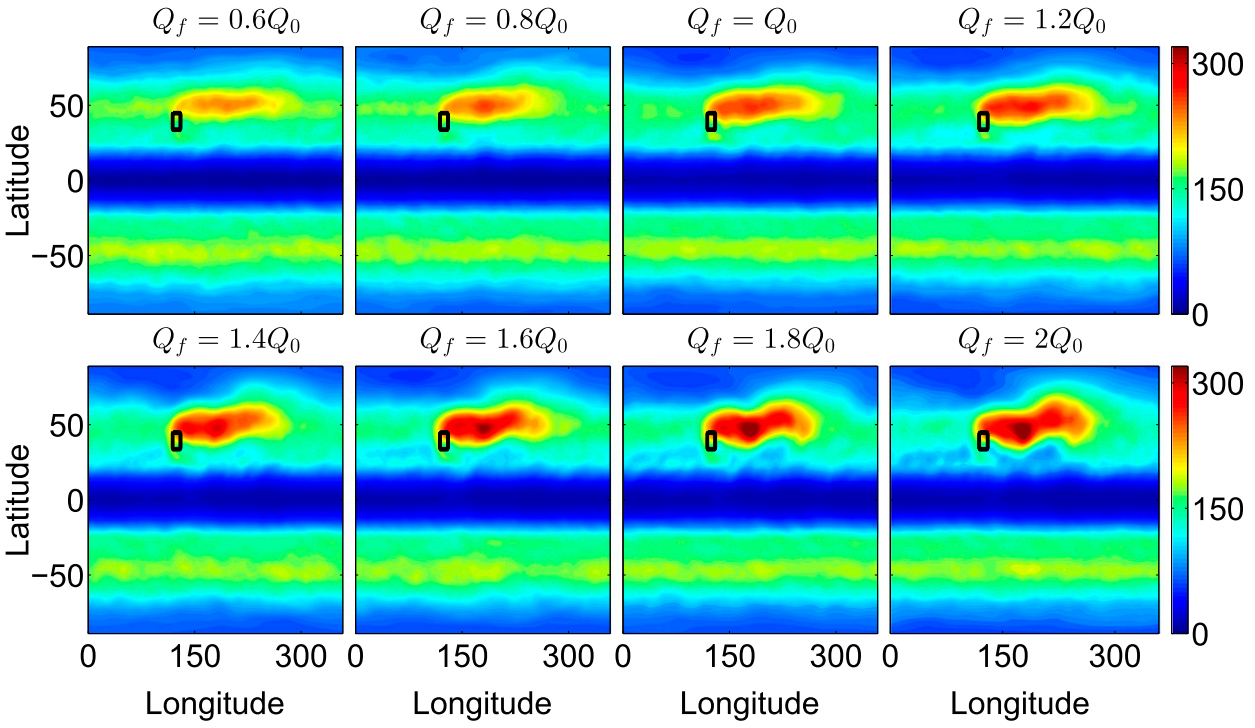

FIG. 8. EKE ($m\,s^{-1}$) at upper levels ($\sigma = 0.3$) for varying strength of the localized oceanic heat flux Q_f ranging from $0.6Q_0$ to $2Q_0$. In all panels, the small thick box shows the region where the localized ocean heat flux is applied.

This contribution is very weak, however, and the overall PV tendency is therefore SW–NE oriented and dominated by the transient nonlinear advection (which is north–south oriented) and the PV tendency due to LHR.

It is hard to infer directly from the SW–NE tilt of the instantaneous PV tendency dipole (Fig. 7a) how much poleward propagation is expected to occur in each of the boxes, as this depends also on the relative position and amplitude of the PV anomaly itself in each of the boxes. One possible measure, which takes this into account, is detailed in the next section. For example, the SW–NE tilt of the instantaneous PV tendency in box D seems to be larger than in box C. However, applying this measure (denoted as the ''poleward index'') to boxes C and D (not shown) reveals that the poleward tendency index is larger in box C than in box D, consistent with the tilt of the averaged cyclonic track, which is also larger in box C (not shown). This is also consistent with the general observed structure of the EKE (Fig. 2a), although it is harder to make a direct connection between the tilt of the EKE and the tilt of the averaged cyclonic track. For example, the EKE appears more zonal or even slightly deflected equatorward in boxes B and D, but this is not reflected in the tilt of the averaged cyclonic track, which is always oriented poleward. Hence, other factors probably also influence the shape of the EKE (see the discussion section).

7. Varying the relative role of the stationary wave

Finally, we examine how the relative role of the stationary wave in advecting the cyclones poleward changes when the strength of the localized heating varies and how that influences the downstream poleward tilt of the storm track. This is done by performing simulations where we systematically increase the strength of the localized ocean heat flux (denoted as Q_f).

Shown here are eight simulations, with a localized heat flux that varies monotonically from $Q_f = 0$ to $Q_f = 2Q_0$ (where $Q_0 = 1500\,W\,m^{-1}$ is the heat flux used for the reference simulation analyzed in the previous sections).[3]

As the heating strength is increased, the EKE at upper levels ($\sigma = 0.3$) becomes both stronger and more tilted toward the pole (Fig. 8). At heating

[3] The value chosen for the reference simulation is somewhat arbitrary and should be taken in a qualitative sense because of the idealized nature of the model used. A larger region of heating convergence would produce a stronger storm track and reduce the values of the heat source needed in order to produce temperature gradients similar to those observed in Earth's storm tracks. The choice of the small heating box is done to keep the zonal asymmetry local with respect to the width of the jet.

strengths weaker than the reference simulation, the poleward tilt of the storm track is barely observed. As the heating increases, a downstream tilt gradually appears. At heating strengths stronger than the reference simulation, there is also an equatorward tilt farther downstream, a manifestation of the wavy structure that appears when the amplitude of the stationary wave increases. Note also that a maximum in the EKE is produced (from $Q_f = 1.4Q_0$ and higher), which is located immediately before the region where the poleward deflection is observed.

Indeed, the tilt angle of the EKE in the downstream region where it deflects poleward increases with the heat flux forcing (Fig. 9a, red dots). In agreement with this, the tilt angle of the averaged cyclonic track increases with the strength of the heating source (Fig. 9a, black dots). Although the deflection angle of the EKE and the tilt of the average cyclone track both increase with the heating source, they are not equal. Without the heat source ($Q_f = 0$), the EKE is obviously zonally symmetric (zero tilt angle), while the cyclones still propagate poleward (tilt angle of approximately 10°). As the heat source is increased, the angles become closer, but they are still not identical.

A detailed examination of the dominant PV terms (viz., latent heat release, transient nonlinear advection, and a stationary advection) for each of the runs, in the downstream region where the tilt is maximized, reveals their relative role in the poleward advection of the cyclones as the heating is increased (Figs. 9b,c). First, the mean value of the PV tendency terms (Fig. 9b) increases as the heating is increased (the mean PV tendency for each term is calculated here as the average over the 25 points with strongest PV tendency values: i.e., around the maximum PV tendency). The enhancement of the mean PV tendency terms is related to the enhancement of the PV anomalies, as a result of the increased localized baroclinicity. Stronger cyclones imply stronger winds, both at upper and lower levels; hence, the nonlinear advection terms can be expected to increase. In addition, stronger cyclones are also associated with stronger upward velocity, so latent heating can be expected to increase as well. Finally, it is not surprising that the stationary advection increases with the heating, since the stationary PV anomaly becomes stronger as the zonal asymmetry increases.

To measure and compare the contribution of each of these PV tendency terms to the poleward propagation of the cyclones, we define an index (denoted as the ''poleward index'') that takes into account both the orientation of the PV tendency and its amplitude with respect to the PV perturbation itself (Fig. 9c). The first point is important since a south–north-oriented PV tendency dipole would contribute more to a poleward propagation than a SW–NE-oriented PV tendency dipole. The second point is important since the same PV tendency would result in a larger poleward drift if the PV perturbation is weak and a smaller poleward drift if the perturbation is strong.

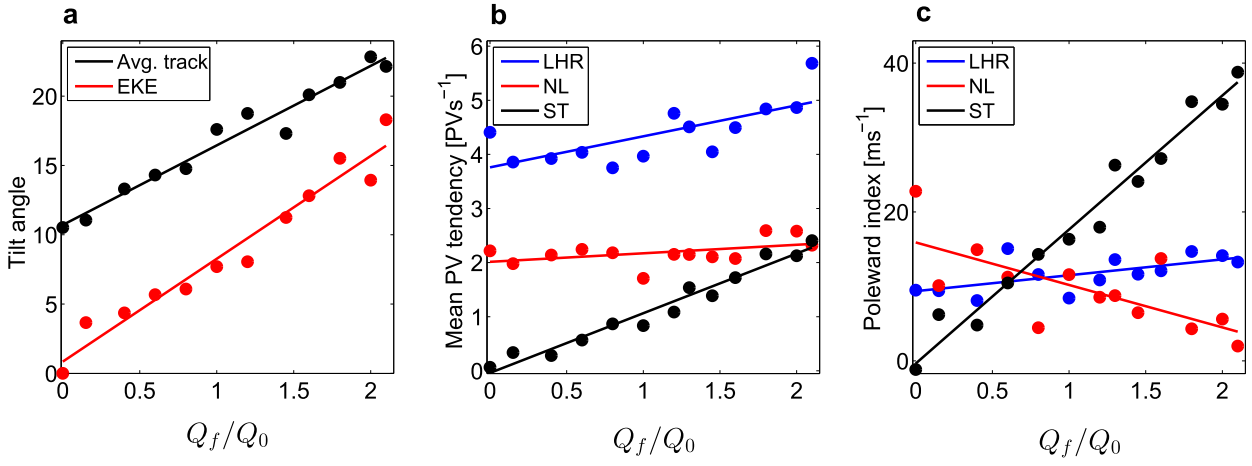

FIG. 9. Simulations with varying heat flux forcing Q_f ranging from 0 to $2.1Q_0$. (a) The tilt angle of the average cyclonic track (°) for cyclones downstream of the heating source (black) and the tilt angle (°) of the EKE with respect to the zonal direction in box C, the downstream region where EKE is most tilted (red), (b) Averaged PV tendency (PVU s^{-1}) calculated in box C for the dominant terms in the PV tendency budget: latent heat release (blue), nonlinear self-advection of the transient perturbations (red), and stationary advection of the transient perturbations (black). (c) The poleward tendency index (m s^{-1}) (see definition in text) for the dominant PV tendency terms as in (b). In each panel, the line shows the linear best fit to the corresponding points, with $R^2 = 0.94$ in (a), $R^2 = 0.51, 0.22, 0.96$ in (b), and $R^2 = 0.38, 0.50, 0.96$ in (c) for LHR, NL, and ST, respectively.

The index is defined as

$$\nu = -\frac{\left\langle \frac{\partial q}{\partial t} \cdot \frac{\partial q}{\partial y} \right\rangle}{\left\langle \frac{\partial q}{\partial y} \cdot \frac{\partial q}{\partial y} \right\rangle}, \tag{6}$$

which is the normalized projection of $\partial q/\partial t$ onto $\partial q/\partial y$, where $\langle\cdot\rangle$ denotes horizontal averaging. The poleward index ν is a scalar with units of meters per second, and it represents the estimated poleward velocity of the q perturbation because of the PV tendency $\partial q/\partial t$ (see appendix B for the full details). Here, $\partial q/\partial t$ is either one of the PV tendency terms.

The poleward index of the dominant PV tendency terms (Fig. 9c) is useful for comparing the relative contribution of each of the PV tendency terms to the poleward propagation. For instance, although the PV tendency associated with latent heat release is strongest (blue dots in Fig. 9b), when taking into account its orientation (which is more eastward than northward), this term appears to be less important for the poleward propagation (blue dots in Fig. 9c), especially at high forcing values. The PV tendency associated with transient nonlinear advection increases modestly as the heat flux strengthens (red dots in Fig. 9b). However, the poleward index of transient nonlinear advection actually decreases with the forcing (red dots in Fig. 9c). This occurs because the amplitude of the PV perturbation itself increases more rapidly than the PV tendency associated with transient nonlinear advection; hence, its overall contribution to the poleward propagation decreases. Finally, although the PV tendency associated with stationary advection is in general weaker than the other two terms, when taking into account its orientation (which is entirely northward), at high heat flux forcing it becomes the most dominant term for the poleward propagation. Hence, when the zonal asymmetry is large, the stationary wave can become an important factor controlling and shaping the structure of the storm track. This is also apparent in the spatial structure of the EKE (Fig. 8), where at high heat flux forcing Q_f, the EKE becomes more wavy, being controlled by the stationary wave.

8. Summary and discussion

In this study, mechanisms controlling the shape of midlatitude storm tracks were investigated using an idealized GCM with a localized heat source, by employing a cyclone-tracking algorithm and constructing PV tendency composites. The inclusion of a localized asymmetry in the midlatitudes results in an enhancement of the EKE and a poleward deflection in the downstream region (Fig. 2).

Transient eddies are known to play an important role in maintaining the poleward tilt of the storm tracks in the time-mean balanced state (Orlanski 1998). However, analyzing the eddy–mean flow interaction in the equilibrium state cannot give a complete understanding of how such a balance is achieved (i.e., it is difficult to infer cause and effect). In the current study we take a different approach to study the poleward deflection of the storm tracks. The idealized GCM output is analyzed with a feature-tracking algorithm to identify cyclones and track them in a Lagrangian sense. Cyclone composites are then produced at various spatial locations downstream of the heating source. The advantage of such a semi-Lagrangian approach is that it allows us to calculate the actual tendency throughout the evolution and propagation of the storms. Thus, the governing mechanisms controlling the motions of cyclones can be identified at different locations and at different stages of their life cycle.

A full PV budget in the downstream region where the tilt is maximized (denoted as box C) highlights three important processes for the poleward propagation: a PV tendency due to diabatic heating associated with LHR, nonlinear advection of the transient perturbation by its own eddy field, and a stationary advection of the transient perturbation. The first two mechanisms for poleward propagation of cyclones are identical to those found in TK16 for a zonally symmetric case, while the last appears only in the case of a localized storm track considered here.

The PV tendency associated with LHR always produces a positive PV tendency in the northeastern side of the low-level PV anomaly, since this is where LHR is maximized. The nonlinear transient PV advection results in a poleward and slightly westward tendency in most of the downstream regions of the storm track, where the interaction with the upper-level PV dominates. This occurs since the upper-level PV, which is always to the west of the low-level PV, induces a poleward velocity on the low-level PV. In the most upstream part of the storm track, however, nonlinear advection is dominated by equatorward low-level advection, probably as a result of the strong diabatically produced low-level PV. Finally, the stationary advection of the transient PV may result in a poleward or an equatorward tendency, depending on the phase of the stationary wave. In the downstream region of the storm track, where the tilt is maximized (box C), all three processes contribute positively to the poleward advection, which explains why the poleward tilt is large in that region.

A systematic variation of the strength of the heating source shows that the storm track becomes more tilted

when the heating is increased and, correspondingly, the poleward deflection of the cyclones increases. The mean value of the dominant PV tendency terms increases with the heating as a result of the increased localized baroclinicity and corresponding enhancement of the PV anomalies. The relative role of the stationary PV advection, measured using a ''poleward index,'' increases significantly when the forcing is increased and becomes the dominant term when the zonal asymmetry is large; it therefore controls the shape of the storm track at high forcing and enhances its downstream poleward tilt.

Note that suggesting a relation between the poleward tilt of the storm track (in the EKE sense) and the tilt of the averaged cyclonic track is only meaningful when a localized asymmetry is present. In the zonally symmetric case, even though cyclones propagate poleward, the EKE is flat. This occurs since storms are being generated equally everywhere; hence, when temporally averaging, the EKE appears zonally symmetric (as in the SH storm track). When a localized asymmetry is present, many cyclones are being generated in the same location and follow a similar path. Therefore, the tilt of the averaged cyclonic track can be expected to correlate with the deflection of the EKE. However, the tilt of the storm track may depend on other factors such as the anticyclones, the spatial distribution of cyclogenesis and moisture, and even the variable chosen to define the storm track (e.g., EKE vs geopotential height variance). In addition, the averaged cyclonic tilt depends strongly on the intensity of storms kept for analysis and the exact region chosen, as well as the variable one uses for defining the storms (e.g., pressure vs vorticity). Hence, while the tilt of the averaged cyclonic track and the poleward deflection of the storm tracks are clearly related, they are not necessarily identical.

The results presented in this study could potentially help us understand the structure of the observed storm tracks on Earth and the differences between them. For example, the Pacific storm track is characterized by a downstream tilt, similar to the results found in this study. The Atlantic storm track appears to be more tilted, and its poleward deflection occurs much farther upstream, closer to the continent on the western boundary. One hypothesis concerns the fact that the two storm tracks differ by their latitudinal positions, which influences the temperature gradients and baroclinicity at the entrance of the storm track (Rivière 2009). In addition, the Atlantic storm track is thought to be more SW–NE tilted because of the shape of the North American continent (Brayshaw et al. 2009). Hence, there is a strong indication that the role of the stationary wave differs in the two storm tracks, which may explain the different structure observed. This issue will be addressed in more detail in a forthcoming paper.

Acknowledgments. We thank Kevin Hodges for his generosity in providing his tracking algorithm and his kind help with implementing it. The authors would also like to thank Edmund Chang, Gwendal Rivière, and an anonymous reviewer, whose comments significantly improved the manuscript. This research has been supported by the Israeli Science Foundation (Grant 1819/16).

APPENDIX A

Decomposition of Horizontal PV Advection Terms

We show here the decomposition of the low-level ($\sigma = 078$) horizontal PV advection in box C, which is the downstream region where the poleward tilt of the storm track is maximized (Fig. 2).

The first six terms on the right-hand side of Eq. (5) are the horizontal advection terms in the zonal direction (Fig. A1). The zonal advection of the transient PV anomaly by the time- and zonal-mean flow, $-[\overline{u}]\partial q'/\partial x$ (Fig. A1a; arrows show the time- and zonal-mean flow), gives a positive PV tendency to the east and negative PV tendency to the west of the low-level transient PV anomaly (black contours). Hence, this term shows the eastward advection of the low-level PV by the eastward zonal flow. The nonlinear advection associated with the transient perturbation itself, $-u'\partial q'/\partial x$ (Fig. A1b), gives a quadrupole structure because of the circular flow pattern associated with the cyclone (arrows). This quadrupole structure would have cancelled out with the meridional nonlinear advection of the transient PV anomaly (Fig. A2b) if the transient velocity field was perfectly axisymmetric (see TK16). The advection of the transient PV anomaly by the stationary zonal flow, $-\overline{u}^*\partial q'/\partial x$ (Fig. A1c; arrows show the stationary flow), also contributes in this region to an eastward advection, though it is weaker in magnitude than the advection by the time- and zonal-mean flow. The first two terms shown here (Figs. A1a,b) are similar in all the downstream regions (i.e., as the cyclone travels downstream). However, the stationary advection of the transient perturbation changes considerably in different locations. The terms involving the advection of the stationary feature (the next three terms) are an order of magnitude smaller than the first three terms shown above. The time- and zonal-mean zonal advection of the stationary PV anomaly ($-[\overline{u}]\partial\overline{q}^*/\partial x$; Fig. A1d) produces as expected a positive PV tendency to its east. The advection of the stationary

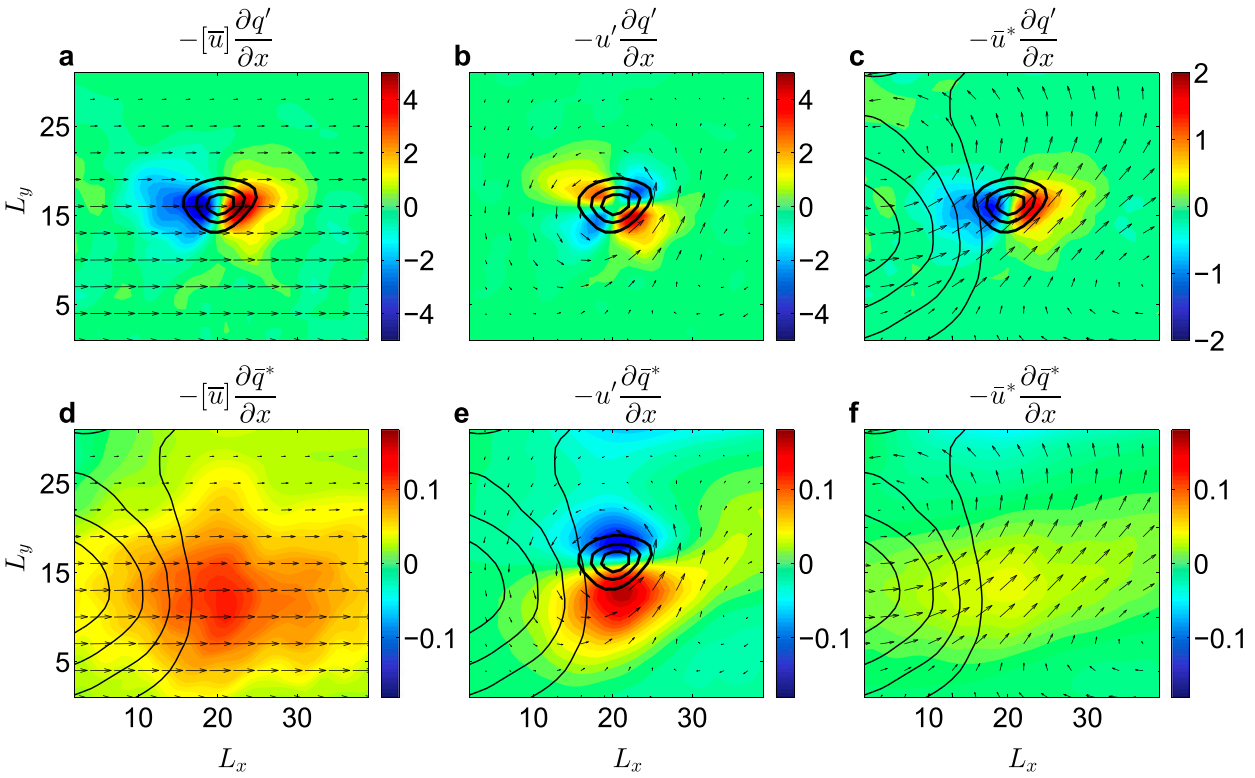

FIG. A1. The low-level ($\sigma = 0.78$) PV tendency associated with the zonal advection terms in box C. Advection of transient PV perturbation by (a) background time- and zonal-mean flow, (b) transient zonal velocity, and (c) stationary zonal velocity; and advection of the stationary PV perturbation by (d) background time- and zonal-mean flow, (e) transient zonal velocity, and (f) stationary zonal velocity. All quantities are normalized by 10^{-6} PVU s^{-1}. The black arrows in each panel show the corresponding advection velocities; (a),(d) the background time- and zonal-mean flow, (b),(e) the transient velocity, and (c),(f) the stationary velocity. Black thick contours in (a)–(c) and (e) show the transient PV anomaly (with lowest contour = 0.1 PVU and contour interval = 0.1 PVU), while black thin contours in (c)–(f) show the stationary PV anomaly (with contours ranging from 0.08 to 0.25 PVU and contour interval = 0.02 PVU). The longitudinal and latitudinal extents of the composite are denoted by L_x and L_y, respectively. The maximum arrow magnitude is 7.1 m s^{-1} in (a),(d); 13.8 m s^{-1} in (b),(e); and 2.8 m s^{-1} in (c),(f).

PV anomaly by the transient perturbation ($-u'\partial q^*/\partial x$; Fig. A1e) creates a dipole that is north–south oriented, a result of the circular velocity associated with the transient PV anomaly. Finally, the nonlinear zonal advection of the stationary PV anomaly with its own PV field ($-\overline{u}^*\partial\overline{q}^*/\partial x$; Fig. A1f) gives a weak eastward advection.

The next six terms on the right-hand side of Eq. (5) are the horizontal advection terms in the meridional direction (Fig. A2). The meridional advection of the time- and zonal-mean flow (which mostly reflects the beta term) by the transient meridional velocity ($-v'\partial[\overline{q}]/\partial y$; Fig. A2a) acts to propagate the transient PV anomaly westward. This is the classical Rossby propagation mechanism: by advecting the background PV (which increases poleward), a positive PV anomaly will produce a positive PV anomaly to its west and a negative PV anomaly to its east, thus propagating westward. The nonlinear meridional advection of the transient PV perturbation by its own field ($-v'\partial q'/\partial y$; Fig. A2b) again gives a quadrupole structure, of opposite sign to the corresponding nonlinear zonal advection term (Fig. A1b). However, the meridional term has an east–west asymmetry; the PV tendencies to its east are much stronger. As discussed in TK16, this asymmetry is a result of the stronger meridional velocity on the eastward side of the cyclone, which is induced from the upper-level PV anomaly. This occurs during the growth stage of the cyclone, since the phase difference between the upper and lower PV anomalies is such that the upper-level winds induce positive poleward velocity at low levels. This was verified in TK16 by performing a piecewise PV inversion, where we showed explicitly the low-level PV advection as a result of the upper-level PV. Indeed, the sum of the nonlinear advection of the transient perturbation by its own field gives a poleward and slightly westward tendency (Fig. 6g). The northwestward tendency was also found in Coronel et al. (2015) (see their Fig. 9b) and was attributed

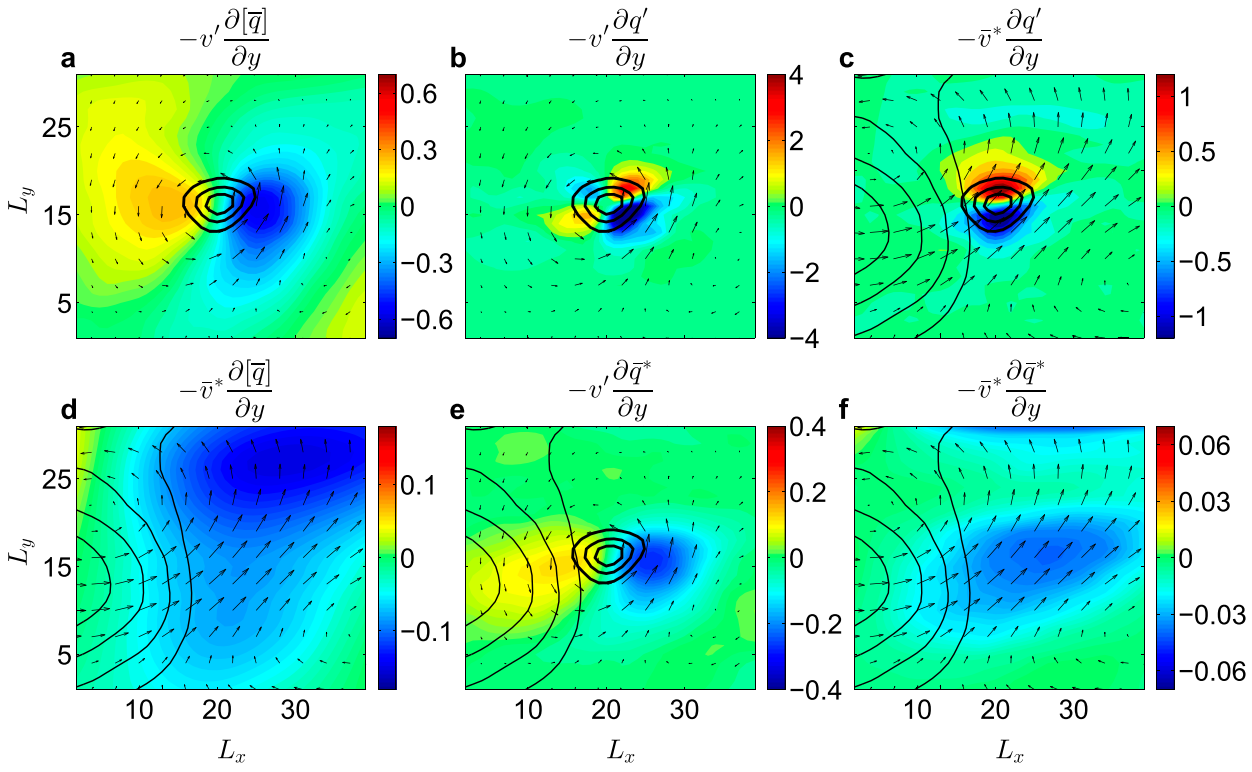

FIG. A2. The low-level ($\sigma = 0.78$) PV tendency associated with the meridional advection terms in box C: (a) advection of the background time- and zonal-mean PV by the transient meridional velocity, (b) nonlinear advection of the transient PV perturbation by the transient meridional velocity, (c) advection of the transient PV perturbation by the stationary meridional velocity, (d) advection of the background time- and zonal-mean PV by the stationary meridional velocity, (e) advection of stationary PV perturbation by the transient meridional velocity, and (f) advection of stationary PV perturbation by the stationary meridional velocity. All quantities are normalized by 10^{-6} PVU s^{-1}. The black arrows in each panel show the corresponding advection velocities; (a),(d) the background time- and zonal-mean flow, (b),(e) the transient velocity, and (c),(f) the stationary velocity. Black thick contours in (a)–(c) and (e) show the transient PV anomaly (with lowest contour = 0.1 PVU, and contour interval = 0.1 PVU), while black thin contours in (c)–(f) show the stationary PV anomaly (with contours ranging from 0.08 to 0.25 PVU, and contour interval = 0.02 PVU). The longitudinal and latitudinal extents of the composite are denoted by L_x and L_y, respectively. The maximum arrow magnitude is 13.8 m s^{-1} in (a), (b), and (e) and 2.8 m s^{-1} in (c), (d), and (f).

to winds induced by the upper-level PV. The meridional advection of the transient PV by the stationary meridional velocity ($-v^*\partial q'/\partial y$; Fig. A2c), in this downstream region of the storm track, gives a poleward PV tendency. As in the zonal advection, the terms involving the meridional advection of the stationary feature are an order of magnitude smaller than those involving the advection by the transient perturbation. The stationary meridional advection of the time- and zonal-mean flow ($-v^*\partial[\overline{q}]/\partial y$; Fig. A2d) is mainly negative, since the stationary meridional velocity in this region is mainly positive. The advection of the stationary PV anomaly by the transient meridional velocity ($-v'\partial q^*/\partial y$; Fig. A2e) creates an east–west-oriented dipole, similar to the meridional advection of the time- and zonal-mean flow. Finally, the stationary meridional advection of the stationary PV anomaly ($-v^*\partial q^*/\partial y$; Fig. A2f) creates a weak and negative PV tendency to the east of the stationary PV.

Note that the terms that involve only the stationary wave (Figs. A1d,f and Figs. A2d,f) do not influence directly the PV tendency of the transient anomaly. Rather, they cancel out with the time-mean value of the forcing associated with diabatic processes $\overline{Q}$ and frictional forces $\overline{F}$. However, these are shown here for completeness.

APPENDIX B

Definition of the Poleward Index

The poleward index of a PV tendency $\partial q/\partial t$, which estimates how much it contributes to a poleward velocity of a PV anomaly q, is found by projecting the PV tendency onto $\partial q/\partial y$. The index can be deduced by decomposing $\partial q/\partial t$ into its symmetrical and asymmetrical parts with respect to the meridional direction y:

$$\frac{\partial q}{\partial t} = \left.\frac{\partial q}{\partial t}\right|_{S(y)} + \left.\frac{\partial q}{\partial t}\right|_{\mathrm{AS}(y)}, \tag{B1}$$

where $S(y)$ and $\mathrm{AS}(y)$ denote symmetrical and asymmetrical with respect to y, respectively.

The asymmetrical part of $\partial q/\partial t$ is involved in poleward propagation and hence can be written as

$$\left.\frac{\partial q}{\partial t}\right|_{\mathrm{AS}(y)} = -v\frac{\partial q}{\partial y}, \tag{B2}$$

where v is the estimated poleward velocity of the q perturbation as a result of the asymmetrical distribution of the PV tendency $\partial q/\partial t$ (v is a scalar with units of meters per second), and it is assumed here that $\partial q/\partial y$ is asymmetrical with respect to y.

The symmetrical part of $\partial q/\partial t$, denoted as $\partial q/\partial t|_{S(y)} = R$ is the residual: that is, the part of $\partial q/\partial t$ that is orthogonal to $\partial q/\partial y$ and hence does not contribute to the poleward tendency.

Multiplying both sides of Eq. (B1) by $\partial q/\partial y$ and performing horizontal integration, denoted with angle brackets, one finds

$$\left\langle \frac{\partial q}{\partial t}\cdot\frac{\partial q}{\partial y}\right\rangle = -v\left\langle \frac{\partial q}{\partial y}\cdot\frac{\partial q}{\partial y}\right\rangle + 0, \tag{B3}$$

since $\iint R(\partial q/\partial y)\,dx\,dy = \int\left[\int R(\partial q/\partial y)\,dy\right]dx = 0$ (an integral over a product of symmetric and asymmetric functions, which is asymmetric, is zero).

Hence, from Eq. (B3), we get

$$v = -\frac{\left\langle \frac{\partial q}{\partial t}\cdot\frac{\partial q}{\partial y}\right\rangle}{\left\langle \frac{\partial q}{\partial y}\cdot\frac{\partial q}{\partial y}\right\rangle}, \tag{B4}$$

which is the projection of $\partial q/\partial t$ onto the asymmetrical distribution that is involved in poleward propagation, normalized by the squared magnitude of the PV perturbation meridional gradient.

The choice of a minus sign in Eq. (B2) can be motivated by noting that

$$\frac{Dq}{Dt} = \frac{\partial q}{\partial t} + u\frac{\partial q}{\partial u} + v\frac{\partial q}{\partial y}, \tag{B5}$$

where Dq/Dt is the change in magnitude or shape of the PV perturbation following the motion of the PV anomaly, which is moving with a velocity (u, v). Rearranging Eq. (B5), we find that $\partial q/\partial t \sim -v\partial q/\partial y$. Hence, the minus sign actually corresponds to a positive meridional velocity, motivating the choice for Eq. (B2).

REFERENCES

Ahmadi-Givi, F., G. C. Graig, and R. S. Plant, 2004: The dynamics of a midlatitude cyclone with very strong latent-heat release. *Quart. J. Roy. Meteor. Soc.*, **130**, 295–323, doi:10.1256/qj.02.226.

Ambrizzi, T., and B. J. Hoskins, 1997: Stationary Rossby-wave propagation in a baroclinic atmosphere. *Quart. J. Roy. Meteor. Soc.*, **123**, 919–928, doi:10.1002/qj.49712354007.

Bengtsson, L., K. Hodges, and E. Roeckner, 2006: Storm tracks and climate change. *J. Climate*, **19**, 3518–3543, doi:10.1175/JCLI3815.1.

Blackmon, M., J. Wallace, N. Lau, and S. Mullen, 1977: An observational study of the Northern Hemisphere wintertime circulation. *J. Atmos. Sci.*, **34**, 1040–1053, doi:10.1175/1520-0469(1977)034<1040:AOSOTN>2.0.CO;2.

Blender, R., K. Fraedrich, and F. Lunkeit, 1997: Identification of cyclone-track regimes in the North Atlantic. *Quart. J. Roy. Meteor. Soc.*, **123**, 727–741, doi:10.1002/qj.49712353910.

Brayshaw, D. J., B. Hoskins, and M. Blackburn, 2008: The storm-track response to idealized SST perturbations in an aquaplanet GCM. *J. Atmos. Sci.*, **65**, 2842–2860, doi:10.1175/2008JAS2657.1.

——, ——, and ——, 2009: The basic ingredients of the North Atlantic storm track. Part I: Land–sea contrast and orography. *J. Atmos. Sci.*, **66**, 2539–2558, doi:10.1175/2009JAS3078.1.

Broccoli, A., and S. Manabe, 1992: The effects of orography on midlatitude Northern Hemisphere dry climates. *J. Climate*, **5**, 1181–1201, doi:10.1175/1520-0442(1992)005<1181:TEOOOM>2.0.CO;2.

Browning, K. A., and N. M. Roberts, 1994: Structure of a frontal cyclone. *Quart. J. Roy. Meteor. Soc.*, **120**, 1535–1557, doi:10.1002/qj.49712052006.

Cai, M., S. Yang, H. M. Van den Dool, and V. E. Kousky, 2007: Dynamical implications of the orientation of atmospheric eddies: A local energetics perspective. *Tellus*, **59A**, 127–140, doi:10.1111/j.1600-0870.2006.00213.x.

Catto, J. L., L. C. Shaffrey, and K. I. Hodges, 2010: Can climate models capture the structure of extratropical cyclones? *J. Climate*, **23**, 1621–1635, doi:10.1175/2009JCLI3318.1.

Chang, E. K. M., S. Lee, and K. L. Swanson, 2002: Storm-track dynamics. *J. Climate*, **15**, 2163–2183, doi:10.1175/1520-0442(2002)015<02163:STD>2.0.CO;2.

Coronel, B., D. Ricard, G. Rivière, and P. Arbogast, 2015: Role of moist processes in the tracks of idealized midlatitude surface cyclones. *J. Atmos. Sci.*, **72**, 2979–2996, doi:10.1175/JAS-D-14-0337.1.

Davis, C. A., 1992: Piecewise potential vorticity inversion. *J. Atmos. Sci.*, **49**, 1397–1411, doi:10.1175/1520-0469(1992)049<1397:PPVI>2.0.CO;2.

——, and K. A. Emanuel, 1991: Potential vorticity diagnostics of cyclogenesis. *Mon. Wea. Rev.*, **119**, 1929–1953, doi:10.1175/1520-0493(1991)119<1929:PVDOC>2.0.CO;2.

——, M. T. Stoelinga, and Y.-H. Kuo, 1993: The integrated effect of condensation in numerical simulations of extratropical cyclogenesis. *Mon. Wea. Rev.*, **121**, 2309–2330, doi:10.1175/1520-0493(1993)121<2309:TIEOCI>2.0.CO;2.

Frierson, D., I. Held, and P. Zurita-Gotor, 2006: A gray-radiation aquaplanet moist GCM. Part I: Static stability and eddy scale. *J. Atmos. Sci.*, **63**, 2548–2566, doi:10.1175/JAS3753.1.

Gilet, J., M. Plu, and G. Rivière, 2009: Nonlinear baroclinic dynamics of surface cyclones crossing a zonal jet. *J. Atmos. Sci.*, **66**, 3021–3041, doi:10.1175/2009JAS3086.1.

Graff, L. S., and J. H. LaCasce, 2014: Changes in cyclone characteristics in response to modified SSTs. *J. Climate*, **27**, 4273–4295, doi:10.1175/JCLI-D-13-00353.1.

Harrold, T. W., 1973: Mechanisms influencing the distribution of precipitation within baroclinic disturbances. *Quart. J. Roy. Meteor. Soc.*, **99**, 232–251, doi:10.1002/qj.49709942003.

Harvey, B. J., L. C. Shaffrey, T. J. Woollings, G. Zappa, and K. I. Hodges, 2012: How large are projected 21st century storm track changes? *Geophys. Res. Lett.*, **39**, L18707, doi:10.1029/2012GL052873.

Held, I. M., 1983: Stationary and quasi-stationary eddies in the extratropical troposphere: Theory. *Large–Scale Dynamical Processes in the Atmosphere*, B. Hoskins and R. Pearce, Eds., Academic Press, 127–168.

——, and M. Ting, 1990: Orographic versus thermal forcing of stationary waves: The importance of the mean low-level wind. *J. Atmos. Sci.*, **47**, 495–500, doi:10.1175/1520-0469(1990)047<0495:OVTFOS>2.0.CO;2.

——, ——, and H. Wang, 2002: Northern winter stationary waves: Theory and modeling. *J. Climate*, **15**, 2125–2144, doi:10.1175/1520-0442(2002)015<2125:NWSWTA>2.0.CO;2.

Hodges, K. I., 1995: Feature tracking on the unit sphere. *Mon. Wea. Rev.*, **123**, 3458–3465, doi:10.1175/1520-0493(1995)123<3458:FTOTUS>2.0.CO;2.

Hoskins, B. J., and D. J. Karoly, 1981: The steady linear response of a spherical atmosphere to thermal and orographic forcing. *J. Atmos. Sci.*, **38**, 1179–1196, doi:10.1175/1520-0469(1981)038<1179:TSLROA>2.0.CO;2.

——, and P. Valdes, 1990: On the existence of storm tracks. *J. Atmos. Sci.*, **47**, 1854–1864, doi:10.1175/1520-0469(1990)047<1854:OTEOST>2.0.CO;2.

——, and T. Ambrizzi, 1993: Rossby wave propagation on a realistic longitudinally varying flow. *J. Atmos. Sci.*, **50**, 1661–1671, doi:10.1175/1520-0469(1993)050<1661:RWPOAR>2.0.CO;2.

——, and K. Hodges, 2002: New perspectives on the Northern Hemisphere winter storm tracks. *J. Atmos. Sci.*, **59**, 1041–1061, doi:10.1175/1520-0469(2002)059<1041:NPOTNH>2.0.CO;2.

——, and ——, 2005: A new perspective on the Southern Hemisphere storm tracks. *J. Climate*, **18**, 4108–4129, doi:10.1175/JCLI3570.1.

——, I. James, and G. White, 1983: The shape, propagation and mean-flow interaction of large-scale weather systems. *J. Atmos. Sci.*, **40**, 1595–1612, doi:10.1175/1520-0469(1983)040<1595:TSPAMF>2.0.CO;2.

Inatsu, M., H. Mukougawa, and S.-P. Xie, 2002: Stationary eddy response to surface boundary forcing: Idealized GCM experiments. *J. Atmos. Sci.*, **59**, 1898–1915, doi:10.1175/1520-0469(2002)059<1898:SERTSB>2.0.CO;2.

Kaspi, Y., and T. Schneider, 2011a: Downstream self-destruction of storm tracks. *J. Atmos. Sci.*, **68**, 2459–2464, doi:10.1175/JAS-D-10-05002.1.

——, and ——, 2011b: Winter cold of eastern continental boundaries induced by warm ocean waters. *Nature*, **471**, 621–624, doi:10.1038/nature09924.

——, and ——, 2013: The role of stationary eddies in shaping midlatitude storm tracks. *J. Atmos. Sci.*, **70**, 2596–2613, doi:10.1175/JAS-D-12-082.1.

Klein, W., 1957: *Principal Tracks and Mean Frequencies of Cyclones and Anticyclones in the Northern Hemisphere*. U.S. Weather Bureau, 60 pp.

Lee, W., and M. Mak, 1996: The role of orography in the dynamics of storm tracks. *J. Atmos. Sci.*, **53**, 1737–1750, doi:10.1175/1520-0469(1996)053<1737:TROOIT>2.0.CO;2.

Macdonald, N. J., 1967: The dependence of the motion of cyclonic and anticyclonic vortices on their size. *J. Atmos. Sci.*, **24**, 449–452, doi:10.1175/1520-0469(1967)024<0449:TDOTMO>2.0.CO;2.

Martin, J., 2006: *Mid-Latitude Atmospheric Dynamics: A First Course*. Wiley, 336 pp.

Mendes, D., and M. D. Mendes, 2004: Climatology of cyclones, anticyclones and storm tracks: Revision of concepts. *Rev. Bras. Geofis.*, **22**, 127–134, doi:10.1590/S0102-261X2004000200003.

Moore, R. W., and M. T. Montgomery, 2005: Analysis of an idealized, three-dimensional diabatic Rossby vortex: A coherent structure of the moist baroclinic atmosphere. *J. Atmos. Sci.*, **62**, 2703–2725, doi:10.1175/JAS3472.1.

——, ——, and H. C. Davies, 2008: The integral role of a diabatic Rossby vortex in a heavy snowfall event. *Mon. Wea. Rev.*, **136**, 1878–1897, doi:10.1175/2007MWR2257.1.

——, ——, and H. Davies, 2013: Genesis criteria for diabatic Rossby vortices: A model study. *Mon. Wea. Rev.*, **141**, 252–263, doi:10.1175/MWR-D-12-00080.1.

Murray, R. J., and I. Simmonds, 1991: A numerical scheme for tracking cyclone centres from digital data. Part I: Development and operation of the scheme. *Aust. Meteor. Mag.*, **39**, 155–166.

Novak, L., M. H. P. Ambaum, and R. Tailleux, 2015: The life cycle of the North Atlantic storm track. *J. Atmos. Sci.*, **72**, 821–833, doi:10.1175/JAS-D-14-0082.1.

O'Gorman, P., and T. Schneider, 2008: The hydrological cycle over a wide range of climates simulated with an idealized GCM. *J. Climate*, **21**, 3815–3832, doi:10.1175/2007JCLI2065.1.

Orlanski, I., 1998: Poleward deflection of storm tracks. *J. Atmos. Sci.*, **55**, 2577–2602, doi:10.1175/1520-0469(1998)055<2577:PDOST>2.0.CO;2.

Oruba, L., G. Lapeyre, and G. Rivière, 2013: On the poleward motion of midlatitude cyclones in a baroclinic meandering jet. *J. Atmos. Sci.*, **70**, 2629–2649, doi:10.1175/JAS-D-12-0341.1.

Parker, D. J., and A. J. Thorpe, 1995: Conditional convective heating in a baroclinic atmosphere: A model of convective frontogenesis. *J. Atmos. Sci.*, **52**, 1699–1711, doi:10.1175/1520-0469(1995)052<1699:CCHIAB>2.0.CO;2.

Peixoto, J. P., and A. H. Oort, 1992: *Physics of Climate*. American Institute of Physics, 520 pp.

Petterssen, S., 1956: *Weather Analysis and Forecasting: Motion and Motion Systems*. Vol. I. McGraw-Hill, 428 pp.

Rivière, G., 2009: Effect of latitudinal variations in low-level baroclinicity on eddy life cycles and upper-tropospheric wave-breaking processes. *J. Atmos. Sci.*, **66**, 1569–1592, doi:10.1175/2008JAS2919.1.

——, P. Arbogast, G. Lapeyre, and K. Maynard, 2012: A potential vorticity perspective on the motion of a mid-latitude winter storm. *Geophys. Res. Lett.*, **39**, L12808, doi:10.1029/2012GL052440.

Sinclair, M., 1997: Objective identification of cyclones and their circulation intensity and climatology. *Wea. Forecasting*, **12**, 595–612, doi:10.1175/1520-0434(1997)012<0595:OIOCAT>2.0.CO;2.

Stoelinga, M. T., 1996: A potential vorticity-based study of the role of diabatic heating and friction in a numerically simulated baroclinic cyclone. *Mon. Wea. Rev.*, **124**, 849–874, doi:10.1175/1520-0493(1996)124<0849:APVBSO>2.0.CO;2.

Tamarin, T., and Y. Kaspi, 2016: The poleward motion of extratropical cyclones from a potential vorticity tendency analysis. *J. Atmos. Sci.*, **73**, 1687–1707, doi:10.1175/JAS-D-15-0168.1.

Trenberth, K. E., 1986: An assessment of the impact of transient eddies on the zonal flow during a blocking episode using localized Eliassen–Palm flux diagnostics. *J. Atmos. Sci.*, **43**, 2070–2087, doi:10.1175/1520-0469(1986)043<2070:AAOTIO>2.0.CO;2.

Vallis, G. K., 2006: *Atmospheric and Oceanic Fluid Dynamics*. Cambridge University Press, 745 pp.

Wallace, J. M., G.-H. Lim, and M. L. Blackmon, 1988: Relationship between cyclone tracks, anticyclone tracks and baroclinic waveguides. *J. Atmos. Sci.*, **45**, 439–462, doi:10.1175/1520-0469(1988)045<0439:RBCTAT>2.0.CO;2.

Williams, L., L. Lee, and S. Son, 2007: Southern Hemisphere spiral jet. *J. Atmos. Sci.*, **64**, 548–563, doi:10.1175/JAS3939.1.

Wills, R. C., and T. Schneider, 2015: Stationary eddies and the zonal asymmetry of net precipitation and ocean freshwater forcing. *J. Climate*, **28**, 5115–5133, doi:10.1175/JCLI-D-14-00573.1.

Wilson, C., B. Sinha, and R. G. Williams, 2010: The shaping of storm tracks by mountains and ocean dynamics. *Weather*, **65**, 320–323, doi:10.1002/wea.633.

Zappa, G., L. C. Shaffrey, and K. I. Hodges, 2013: The ability of CMIP5 models to simulate North Atlantic extratropical cyclones. *J. Climate*, **26**, 5379–5396, doi:10.1175/JCLI-D-12-00501.1.

Zishka, K. M., and P. J. Smith, 1980: The climatology of cyclones and anticyclones over North America and surrounding ocean environs for January and July, 1950–77. *Mon. Wea. Rev.*, **108**, 387–401, doi:10.1175/1520-0493(1980)108<0387:TCOCAA>2.0.CO;2.